A computationally-efficient micromechanical model for the fatigue life of unidirectional composites under tension-tension loading

Marco Alves, Soraia Pimenta*

Department of Mechanical Engineering, South Kensington Campus, Imperial College, London, SW7 2AZ, United Kingdom

Abstract

Failure of fibre-reinforced composites is affected by fatigue, which increases the challenge in designing safe and reliable composite structures. This paper presents an analytical model to predict the fatigue life of unidirectional composites under longitudinal tension-tension. The matrix and fibre-matrix interface are represented through a cohesive constitutive law, and a Paris law is used to model fatigue due to interfacial cracks propagating from fibre-breaks. The strength of single-fibres is modelled by a Weibull distribution, which is scaled hierarchically though a stochastic failure analysis of composite fibre-bundles, computing stochastic S-N curves of lab-scaled specimens in less than one minute. Model predictions are successfully validated against experiments from the literature. This model can be used to reduce the need for fatigue testing, and also to evaluate the impact of constituent properties on the fatigue life of composites.

Keywords: Micro-mechanics, Analytical modelling, Cohesive interface modelling, Fibre reinforced material, Fatigue

1. Introduction

Many studies have shown that composite materials are sensitive to cyclic degradation, as experimental results show a significant reduction in the stiffness and strength of composites with the increasing number of fatigue cycles applied, both under simple and more complex loading cases [1–11]. Due to limited capabilities to predict the behaviour of composites across their entire life-time, large safety factors are often employed, leading to inefficient and over-designed components. It is therefore critical to be able to predict the life span of composites under cyclic loading, since fatigue is one of the main failure mechanisms in engineering structures (such as pressure vessels and aircraft components) [12].

Fibre-reinforced composites are inhomogeneous by nature and have a more complex behaviour than that of homogeneous materials, since different types of damage can occur in the different constituents; this fact makes the life-time prediction of composite materials a challenging task. Carbon fibres have an elastic behaviour and are generally considered to be insensitive to fatigue effects [13]; however, even a UniDirectional (UD) Carbon-Fibre Reinforced Polymer (CFRP) is vulnerable to degradation under tension-tension cyclic loading, due to the formation of damage in the matrix and in the fibre-matrix interface [14, 15].

*Corresponding author

Email addresses: marco.alves@imperial.ac.uk (Marco Alves), soraia.pimenta@imperial.ac.uk (Soraia Pimenta)

When a UD composite is loaded under uniform tension, due to the stochastic nature of the strength of single-fibres, dispersed breaks of the weaker fibres occur; these fibre-breaks generate stress concentrations in the neighbouring fibres, increasing their failure probability, which leads to progressive accumulation and clustering of fibre-breaks. The presence of these fibre- and cluster-breaks causes local shear damage of the matrix and/or fibre-matrix interface [1, 15]; consequently, under cyclic loading (and if the composite survived the first load cycle), the matrix and/or fibre-matrix interface surrounding the broken fibres will start do degrade further, and interfacial debonds start to grow [1, 16]. This will increase the stress concentrations in the surrounding fibres along a longer distance, which eventually may lead to failure of the composite.

Talreja [15] introduced the concept of a "fatigue-life diagram" for the interpretation of the S-N curves of UD composites, which clearly distinguishes three regions: region-I, defined by a horizontal scatter band centred at the composite static failure strain or stress, dominated by fibre failure; region-II, characterised by a scatter band with a double-logarithmic relationship between the peak stress applied and the number of fatigue cycles to failure, dominated by progressive damage in the matrix and/or in the fibre-matrix interface; and region-III, that defines a region of no fatigue failure, governed by the fatigue limit of the matrix and fibre-matrix interface.

The growth rate of matrix cracks and interfacial debonds can be modelled by a Paris power law [17–20], and is affected by the quality of the bonding between the fibres and the matrix, which is often controlled by surface treatments on the fibres [6, 21, 22]. Determining the Paris law constants for crack propagation along the fibre-matrix interface is a challenging task: in the literature, a wide scatter of data can be found for the values of Paris law constants for mode-II debonding/delamination in composite materials [16, 23–27]; moreover, there are also only a few experimental studies for the Paris law constants for interfacial debonding around individual fibres [28] and no experimental data for debonding around small bundles of fibres.

Fibre Bundle Models (FBMs) are a classical approach to predict the quasi-static tensile failure process of UD composites and the associated size effects. Most of the existing FBMs use simple constitutive laws for the matrix/interface behaviour (e.g. linear-elastic [29, 30], perfectly-plastic [31, 32], elastic-plastic [33, 34] and pre-debonded [35, 36]). More realistic behaviours of the matrix/interface (with a finite value of both the strength and toughness) have been implemented through Finite Element Analysis (FEA), where cohesive elements have been used to study delamination and debonding in composite materials both under static and fatigue loading [20, 37–42]; however, such FE simulations have a high computational cost, and are therefore not suitable to simulate the micromechanics of longitudinal tensile failure of UD composites under cyclic load.

Only a few micromechanical approaches to predict fatigue of UD composite under cyclic longitudinal tension can be found in the literature. Ogin [43] used an analytical approach to predict the lifetime and residual strength of both UD and cross-ply composite laminates, by taking into account the fatigue growth of fibre/matrix interface debonds, as well as the statistical distribution of flaws along the fibres; however, the model neglected the formation of clusters of fibre-breaks, which has been recently shown to affect the failure process under fatigue [44]. Qian et al. [37] developed a FE fatigue model for UD composites, where the fatigue damage of unit-cells with 7 and 45 fibres was analysed and, with a multi-scale approach, the fatigue life of coupon-sized specimens were predicted; the model, besides being computationally expensive, also over-estimated the fatigue life of the coupons.

Overall, there is a lack of models in the literature able to accurately and efficiently predict the fatigue response of UD composites under longitudinal tension. Therefore, this study proposes an analytical model to predict the fatigue life and the associated size effects of UD CFRPs under longitudinal tension-tension cyclic loading. The model considers interfacial debonds

---

Nomenclature

Uppercase roman variables

A	cross-sectional area
C_K	stress concentration strength parameter
$C_{\mathrm{int}}^{\mathrm{II}}$	Paris law constant
E	tensile modulus
G	shear modulus
$\mathcal{G}_{\mathrm{int}}^{\mathrm{IIc}}$	critical energy release rate
$\mathcal{G}_{\mathrm{int}}^{\mathrm{IIth}}$	threshold energy release rate
N	fatigue cycle number
P	perimeter
S	survival probability
F	failure probability
T	characteristic thickness
U	dissipated energy

Lowercase roman variables

a	crack length
d	damage parameter
k	stress concentration factor
l	length
m	Weibull shape parameter
$m_{\mathrm{int}}^{\mathrm{II}}$	Paris law exponent
t	thickness

Lowercase greek variables

γ	shear strain
λ	shear-lag numerical constant
σ	longitudinal stress
τ	shear stress
ϕ	fibre diameter

Subscripts

$\mathcal{A}$	fibre/sub-bundle $\mathcal{A}$
$\mathcal{B}$	fibre/sub-bundle $\mathcal{B}$
c	control length
crt	critical
debond	debonded phase
e	effective recovery length
fd	fully debonded
init	initiation phase
int	pristine interface properties
K	linear stress concentrations field
$\mathcal{K}$	one sub-bundle fails and the other survives
L	linear stress field
peak	
prop	propagation phase
r	reference length
s	static
spec	specimen
trough	lowest value of the cyclic load
U	uniform
$\mathcal{U}$	both sub-bundles survive

Superscripts

∞	remote
f	fibre
i	bundle level

---

propagating from fibre-breaks as the main fatigue mechanism, where the debond/crack growth rate is governed by the Paris law (Section 2.3). This gradual fatigue degradation of the matrix/interface under fatigue is coupled with an analytical micromechanical hierarchical fibre bundle model, in order to capture cyclic effects on the longitudinal tensile strength of UD carbon-fibre composites (Section 2.4). The model allows for the determination of probabilistic S-N curves and associated size effects, and is validated against experimental results in Section 3. The findings and results of the model are discussed in Section 4, and the main conclusions are drawn in Section 5.

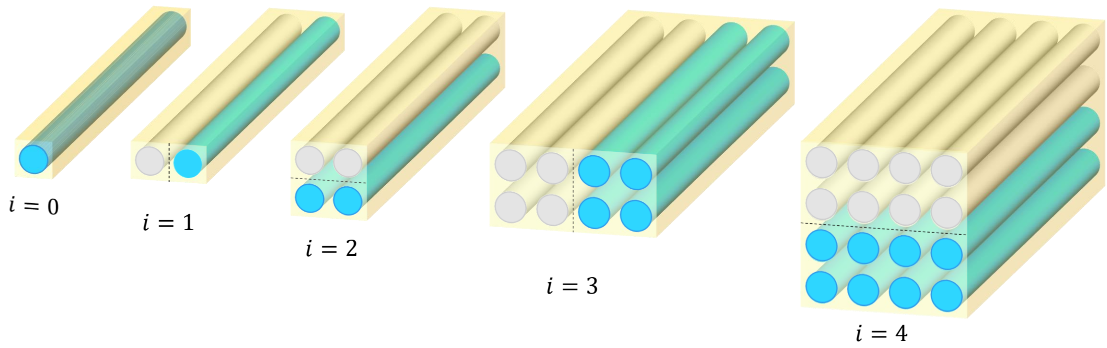

Figure 1: Hierarchical fibre bundles built in a square fibre arrangement [32].

2. Fatigue Model

2.1. Model idealisation

The overall strategy of the model developed in this paper is an extension of the Hierarchical Scaling Law (HSL) for the static strength of composite fibre bundles [32], and its general assumptions are the following:

(i) Hierarchical fibre bundles are generated by paring two level-[0] bundles (single fibres) into a level-[1] bundle and, through a recursive process, pairing two level-[i] bundles into one level-[$i + 1$] bundle (Figure 1) [32, 35]. The number of fibres $n^{[i]}$ in a level-[i] bundle is given by

$$n^{[i]} = 2^i \qquad \Leftrightarrow \qquad i = \log_2 n^{[i]}. \tag{1}$$

(ii) Bundle failure propagates hierarchically in a self-similar way, assuming that the failure process of bundles of different scales are governed by the same mechanisms [45, 46]. This way, the mathematical description of the failure of a level-[1] bundle (with 2 individual fibres), hereby designated as scaling law, can be used to describe the failure process of any level-[i] bundle. The scaling law to be developed for fatigue loading is detailed in Section 2.4.

(iii) The fibres are assumed to resist longitudinal stresses [29, 32, 35] and to be fatigue insensitive [13]. The strength of a single fibre under a uniform stress field σ^∞ is given by a Weibull distribution, defined by the shape parameter m and scale parameter σ_0^f, measured at a reference length l_0^f [47]. This way, the survival probability of a single fibre ($S_\mathrm{U}^{[0]}$) under a uniform stress σ^∞ can be defined and scaled to any length l by the Weakest Link Theory (WLT):

$$S_{\mathrm{U},l}^{[0]}(\sigma^\infty) = \exp\left[-\frac{l}{l_0^\mathrm{f}} \cdot \left(\frac{\sigma^\infty}{\sigma_0^\mathrm{f}}\right)^m\right]. \tag{2}$$

(iv) The matrix and/or fibre-matrix interface is responsible for the stress redistribution in the proximity of a fibre or sub-bundle-break, governed by shear-lag [48]. This shear-lag behaviour is represented by one single cohesive law (Figure 3) [39], which combines the response of the matrix and fibre-matrix interface; accordingly, the matrix and fibre-matrix interface will hereafter be simply referred to as the "interface". The interface will be subjected to both static and fatigue damage initiated from fibre-breaks, leading to debonding. The static damage (initiated in the first loading cycle) will be analysed in Section 2.2, and the fatigue damage will be governed by a Paris power law [17–20], as detailed in Section 2.3.

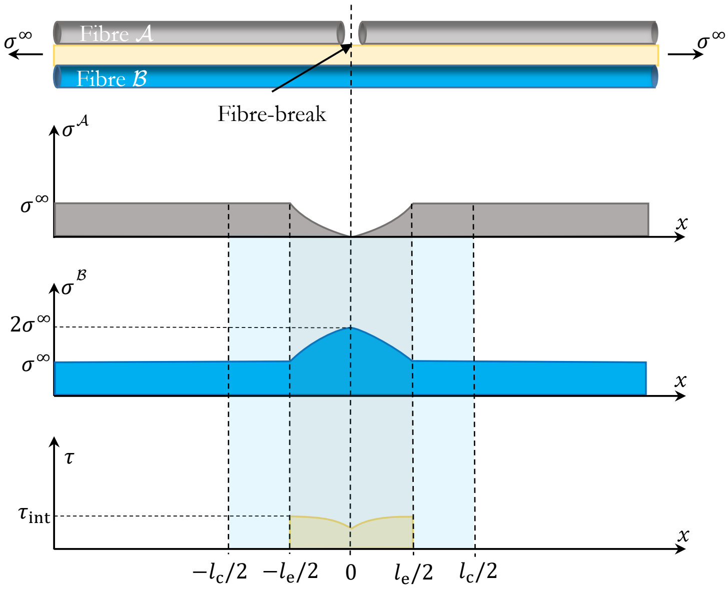

Figure 2: Static stress fields and length scales near a fibre-break within a level-[1] bundle.

(v) The length required for a broken level-$[i]$ sub-bundle in the composite to recover the applied remote stress defines the *effective recovery length* $l_{\mathrm{e}}^{[i]}$, as well as the *control region* (with length $l_{\mathrm{c}}^{[i+1]}$) within which breaks in neighbouring level-$[i]$ sub-bundles interact with each other (Figure 2). The increase of the effective recovery and control lengths with the increasing number of loading cycles (N) will be the main fatigue damage mechanism considered in this model [15].

2.2. Static stress fields near a fibre-break considering a cohesive interface

During the first loading cycle, the remote stress σ^{∞} will cause the break of the weaker fibres, according to the Weibull distribution characterising the stochastic single-fibre strength (defined in Eq. 2). This will generate local stress concentrations in the surviving fibres and shear stresses in the interface, as illustrated in Figure 2 for a 2-fibres (i.e. level-[1]) bundle. This section will analyse the stress fields generated in the neighbourhood of a fibre or sub-bundle break during the first loading cycle (i.e. at $N = 0$, before the onset of fatigue effects), considering that the shear behaviour of the interface can be described by the linear cohesive law shown in Figure 3.

The choice of a linear cohesive law for the shear-lag stress transfer is motivated by two reasons: firstly, it accounts for the finite value of both the strength and the toughness of the interface between fibres, and is therefore more realistic than simpler constitutive laws [31–34] previously used in the literature. Secondly, the Paris law used to predict damage propagation under fatigue is usually formulated in energy-based terms [43, 49], and therefore cannot be applied to the perfectly-plastic interface behaviour assumed in the original static formulation of the HSL [32]. The cohesive behaviour of the interface (see Figure 3) is defined by the mode-II fracture toughness $\mathcal{G}_{\mathrm{int}}^{\mathrm{IIc}}$, shear strength τ_{int}, and by the interface thickness t_{int} (which can be calculated from the average matrix thickness between the fibres in a square arrangement, see Appendix A [32]).

The maximum shear strain γ_{int} and the shear tangent stiffness G_{int} of the cohesive law are

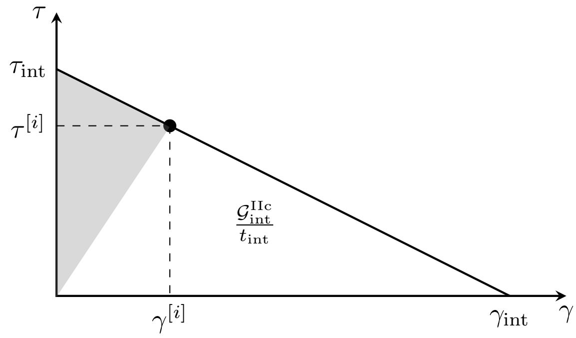

Figure 3: Linear cohesive law of the interface under static shear stresses.

defined as follows:

$$\gamma_{\mathrm{int}} = \frac{2\mathcal{G}_{\mathrm{int}}^{\mathrm{IIc}}}{\tau_{\mathrm{int}} \cdot t_{\mathrm{int}}}, \tag{3a}$$

$$G_{\mathrm{int}} = -\frac{\tau_{\mathrm{int}}}{\gamma_{\mathrm{int}}} = -\frac{\tau_{\mathrm{int}}^2 \cdot t_{\mathrm{int}}}{2\mathcal{G}_{\mathrm{int}}^{\mathrm{IIc}}}. \tag{3b}$$

In order to model interfacial debonding through an analytical implementation of this cohesive behaviour, the stress fields near a fibre or sub-bundle break are required. Therefore, Pimenta and Robinson's [50] analytical shear-lag model is here applied within the effective recovery length of a level-$[i]$ broken sub-bundle (as shown in Figure 2 for $i = 0$), leading to the following differential equation [50]:

$$\frac{\mathrm{d}^2 \Delta\sigma^{[i]}(x)}{\mathrm{d}x^2} = -{\lambda^{[i]}}^2 \cdot \Delta\sigma^{[i]}(x), \quad \text{with } \lambda^{[i]} = \sqrt{\frac{2|G_{\mathrm{int}}|}{T^{[i]} \cdot t_{\mathrm{int}} \cdot E^{\mathrm{f}}}} = \frac{\tau_{\mathrm{int}}}{\sqrt{T^{[i]} \cdot E^{\mathrm{f}} \cdot \mathcal{G}_{\mathrm{int}}^{\mathrm{IIc}}}}, \tag{4}$$

where $\Delta\sigma^{[i]}$ is the stress difference between the level-$[i]$ sub-bundles $\mathcal{B}$ (surviving) and $\mathcal{A}$ (broken), E^{f} is the Young's modulus of a single fibre, and $T^{[i]}$ is the equivalent shear-lag thickness of the level-$[i]$ sub-bundle, defined by the ratio between its cross-sectional area $A^{[i]}$ and the perimeter $P^{[i]}$ (see Appendix A). Following the stress fields shown in Figure 2, the boundary conditions for the differential equation can be defined as follows:

$$\Delta\sigma^{[i]}(x = l_{\mathrm{e}}^{[i]}/2) = 0, \tag{5a}$$

$$\Delta\sigma^{[i]}(x = 0) = 2\sigma^{\infty}, \tag{5b}$$

$$\tau^{[i]}(x = l_{\mathrm{e}}^{[i]}/2) = \tau_{\mathrm{int}}. \tag{5c}$$

Considering the boundary conditions in Eq. 5, the solution of Eq. 4 allows one to define the following analytical stress field distributions:

$$\Delta\sigma^{[i]}(x) = \frac{2\tau_{\text{int}}}{\lambda^{[i]} \cdot T^{[i]}} \cdot \sin\Big(\lambda^{[i]}\Big[\frac{l_{\text{e}}^{[i]}}{2} - x\Big]\Big), \tag{6a}$$

$$\sigma^{\mathcal{A}}(x) = \sigma^{\infty} - \frac{\tau_{\text{int}}}{\lambda^{[i]} \cdot T^{[i]}}\sin\Big(\lambda^{[i]}\Big[\frac{l_{\text{e}}^{[i]}}{2} - x\Big]\Big), \tag{6b}$$

$$\sigma^{\mathcal{B}}(x) = \sigma^{\infty} + \frac{\tau_{\text{int}}}{\lambda^{[i]} \cdot T^{[i]}}\sin\Big(\lambda^{[i]}\Big[\frac{l_{\text{e}}^{[i]}}{2} - x\Big]\Big), \tag{6c}$$

$$\tau^{[i]}(x) = \tau_{\text{int}} \cdot \cos\Big(\lambda^{[i]}\Big[\frac{l_{\text{e}}^{[i]}}{2} - x\Big]\Big). \tag{6d}$$

The stress fields defined in Eq. 6 are valid only below a critical remote stress ($\sigma_{\text{crt}}^{\infty}$), above which the energy release rate associated with the propagation of a crack along the interface (initiating from a sub-bundle break) is higher than its fracture toughness $\mathcal{G}_{\text{int}}^{\text{IIc}}$. This critical remote stress depends on the level of the broken sub-bundle, and is given by [50]

$$\sigma_{\text{crt}}^{\infty[i]} = \sqrt{\frac{\mathcal{G}_{\text{int}}^{\text{IIc}} \cdot E^{\text{f}}}{T^{[i]}}}. \tag{7}$$

From the analytical stress fields near a fibre or sub-bundle-break defined in Eq. 6, the effective recovery length associated to the first loading cycle (i.e. under static loading with $N = 0$) can be obtained by imposing the boundary condition presented in Eq. 5b to the stress field defined in Eq. 6a:

$$\frac{l_{\text{e}}^{[i]}(\sigma^{\infty}, N = 0)}{2} = \frac{1}{\lambda^{[i]}} \cdot \text{asin}\left(\frac{\sigma^{\infty}}{\sigma_{\text{crt}}^{\infty[i]}}\right). \tag{8}$$

This effective recovery length allows one to determine the shear stress at the critical point ($x = 0$) of the level-$[i]$ sub-bundle interface from Eq. 6d:

$$\tau_{\text{crt}}^{[i]}(\sigma^{\infty}, 0) = \tau_{\text{int}}\sqrt{1 - \left(\frac{\sigma^{\infty}}{\sigma_{\text{crt}}^{[i]}}\right)^2}. \tag{9}$$

2.3. Fatigue damage model for the interface

The stress fields defined in Section 2.2 are valid during the first loading cycle, as the remote load is applied to the fibre bundle up to $\sigma^{\infty} = \sigma_{\text{peak}}^{\infty}$; after this, cyclic loading takes place with a stress ratio $R^{\infty} = \sigma_{\text{trough}}^{\infty}/\sigma_{\text{peak}}^{\infty}$, where $\sigma_{\text{peak}}^{\infty}$ and $\sigma_{\text{trough}}^{\infty}$ are the peak and trough remote stresses applied during one fatigue cycle, respectively. During the cyclic loading, a mode-II interfacial crack may eventually be initiated from a sub-bundle break (at $x = 0$ in Figure 2), as will be described in Section 2.4; with further fatigue cycles, the crack growth rate, represented here by $\partial A^{[i]}/\partial N$ (where N is the number of fatigue cycles applied), is given by the Paris law as follows [16, 39, 51]:

$$\frac{\partial A^{[i]}(\sigma_{\text{peak}}^{\infty}, R^{\infty})}{\partial N} = \begin{cases} C_{\text{int}}^{\text{II}}\left(\frac{\Delta\mathcal{G}_{\text{II}}^{[i]}(\sigma_{\text{peak}}^{\infty}, R^{\infty})}{\mathcal{G}_{\text{int}}^{\text{IIc}}}\right)^{m_{\text{int}}^{\text{II}}} & \text{if } \mathcal{G}_{\text{int}}^{\text{IIth}} < \mathcal{G}_{\text{peak}}^{[i]}(\sigma_{\text{peak}}^{\infty}) < \mathcal{G}_{\text{int}}^{\text{IIc}}, \\ 0 & \text{otherwise.} \end{cases} \tag{10}$$

This formulation of the Paris law requires three parameters characterising the mode-II fatigue response of the interface: $C_{\text{int}}^{\text{II}}$ and $m_{\text{int}}^{\text{II}}$ are the Paris law constants, and $\mathcal{G}_{\text{int}}^{\text{IIth}}$ is the threshold mode-II energy release rate (below which no fatigue occurs). The term $\mathcal{G}_{\text{peak}}^{[i]}$ is the mode-II energy release rate applied to the crack-tip of the interface of a broken level-$[i]$ sub-bundle, and $\Delta\mathcal{G}_{\text{II}}^{[i]}$ is the variation of the energy release rate between the peak and trough of the loading cycle.

During the propagation of a mode-II interfacial crack around a broken level-$[i]$ sub-bundle, it can be shown that the energy release rate at the crack-tip is constant and independent of the crack length by assuming a shear-lag stress transfer (leading to a self-similar crack growth [20]) and, for this reason, $\mathcal{G}_{\text{peak}}^{[i]}$ and $\Delta\mathcal{G}_{\text{II}}^{[i]}$ can be obtained by rearranging the definition of $\sigma_{\text{crt}}^{\infty[i]}$ in Eq. 7:

$$\mathcal{G}_{\text{peak}}^{[i]}(\sigma_{\text{peak}}^{\infty}) = \frac{T^{[i]} \cdot (\sigma_{\text{peak}}^{\infty})^2}{E^{\text{f}}} \quad \text{and} \quad \Delta\mathcal{G}_{\text{II}}^{[i]}(\sigma_{\text{peak}}^{\infty}, R^{\infty}) = \frac{T^{[i]}\left[(\sigma_{\text{peak}}^{\infty})^2 \cdot (1 - R^{\infty 2})\right]}{E^{\text{f}}}. \tag{11}$$

Associated with $\mathcal{G}_{\text{int}}^{\text{IIth}}$ is the threshold remote peak stress $\sigma_{\text{th}}^{\infty[i]}$, below which the interface of a level-$[i]$ sub-bundle does not undergo any fatigue damage, given by

$$\sigma_{\text{th}}^{\infty[i]} = \sqrt{\frac{\mathcal{G}_{\text{int}}^{\text{IIth}} \cdot E^{\text{f}}}{T^{[i]}}}. \tag{12}$$

Although the Paris law is usually used to model propagation of fatigue damage once a crack-tip is formed (for the interface near a level-$[i]$ sub-bundle break, this condition corresponds to $\tau^{[i]}(\sigma_{\text{peak}}^{\infty}, x = 0) = 0$), the fact that the crack propagation is self-similar suggests that the degradation of the interface before the initiation of a crack-tip can also be modelled by the Paris law. Neglecting the magnification of the energy release rate near the proximity of the fibre-break [20], the growth of the effective recovery length — within which the interface is either partially damaged or fully debonded — will therefore be described by the Paris law, defined in Eq. 10, both before (Figure 2) and after (Figure 4) the initiation of a crack-tip at $x = 0$. Combining this assumption with a cycle jump strategy [39] suitable for high-cycle fatigue modelling, the effective recovery length is calculated as follows:

$$\frac{l_{\text{e}}^{[i]}(\sigma_{\text{peak}}^{\infty}, R^{\infty}, N + \Delta N)}{2} = \frac{l_{\text{e}}^{[i]}(\sigma_{\text{peak}}^{\infty}, R^{\infty}, N)}{2} + \frac{1}{P^{[i]}} \cdot \frac{\mathrm{d}A^{[i]}}{\mathrm{d}N}(\sigma_{\text{peak}}^{\infty}, R^{\infty}) \cdot \Delta N, \tag{13}$$

where ΔN is the cycle jump (a convergence study of the cycle jump size will be presented in Section 3.2). This growth of the effective recovery length leads to changes in the stress fields of the sub-bundles and the interface near fibre-breaks, as will be derived in Section 2.4 and shown in Figures 4 and 5.

2.4. Fatigue strength model

The static strength model for hierarchical fibre bundles [32] will be extended in this section to capture the strength degradation due to cyclic loading. The analysis of the effective recovery length evolution — characterised by Eq. 13 — will be divided in three phases: crack initiation (Figure 2), crack propagation (Figure 4), and fully debonded state (Figure 5).

2.4.1. Crack initiation phase

During the crack initiation phase, the interface's ability to transfer shear stresses near fibre-breaks will gradually be reduced with progressive cyclic loading, leading to an increase in the recovery length governed by the Paris law 13. After a given number ($N_{\text{init}}^{[i]}$) of fatigue cycles, the amount of interface damage accumulated near the fibre-breaks (at $x = 0$) becomes sufficient to initiate an interfacial crack-tip, which defines the end of the crack initiation phase.

An interfacial crack-tip near a broken level-$[i]$ sub-bundle is characterised by an interface shear-stress $\tau^{[i]}(x = 0, N) = 0$. This condition would also be verified in the first loading cycle under

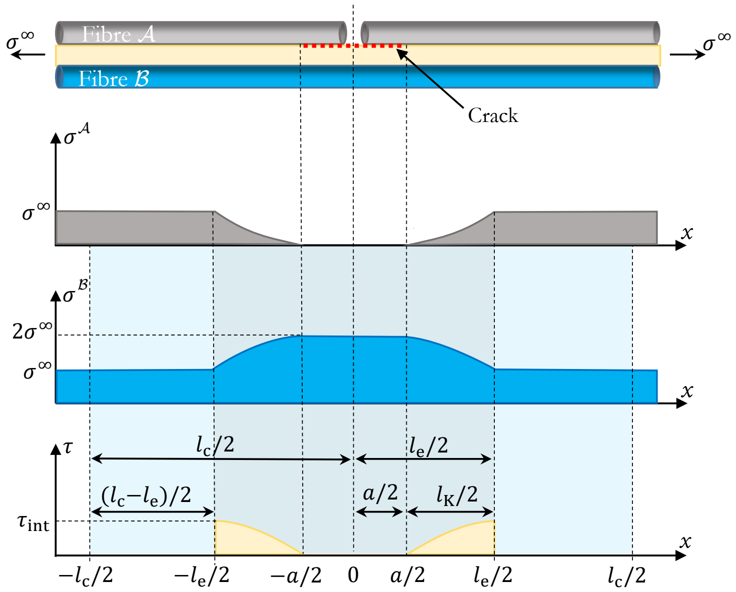

Figure 4: Stress fields and length scales in a level-[1] bundle during the crack propagation phase.

the critical stress $\sigma^\infty_{\text{peak}} = \sigma^{\infty[i]}_{\text{crt}}$ (as defined in Eq. 7); the critical effective recover length $l^{[i]}_{\text{K}}$ which corresponds to this critical static case can be calculated analytically through Eq. 8 as

$$l^{[i]}_{\text{K}} = l^{[i]}_{\text{e}}(\sigma^{\infty[i]}_{\text{crt}}, N = 0) = \frac{\pi}{2\lambda^{[i]}}. \tag{14}$$

The number of cycles required for the crack initiation phase ($N^{[i]}_{\text{init}}$) around a level-[i] sub-bundle can then be calculated by combining the definition of the critical value of the effective recovery length (Eq. 14) and the Paris law evolution (Eq. 13):

$$\begin{aligned} \frac{l^{[i]}_{\text{K}}}{2} &= \frac{l^{[i]}_{\text{e}}(\sigma^\infty_{\text{peak}}, 0)}{2} + \frac{1}{P^{[i]}} \cdot \frac{\mathrm{d}A^{[i]}}{\mathrm{d}N}(\sigma^\infty_{\text{peak}}, R^\infty) \cdot N^{[i]}_{\text{init}} \\ \Leftrightarrow \quad N^{[i]}_{\text{init}} &= \frac{\left(\frac{1}{\lambda} \cdot \left[\operatorname{asin}\left(\frac{\sigma^\infty_{\text{peak}}}{\sigma^{\infty[i]}_{\text{crt}}}\right) - \frac{\pi}{2}\right]\right) \cdot P^{[i]}}{\frac{\mathrm{d}A^{[i]}}{\mathrm{d}N}(\sigma^\infty_{\text{peak}}, R^\infty)}. \end{aligned} \tag{15}$$

Eq. 15 is valid if $\sigma^\infty_{\text{peak}} < \sigma^{\infty[i]}_{\text{crt}}$, in which case a crack-tip will not be formed during the static loading (i.e. $\tau^{[i]}(x = 0, N = 0) > 0$); in this case, at the end of $N^{[i]}_{\text{init}}$ loading cycles, a crack will start propagating from the critical point ($x = 0$) of the level-[i] interface of a broken sub-bundle. If the peak remote stress applied to the bundle exceeds the value of $\sigma^{\infty[i]}_{\text{crt}}$, unstable crack propagation is sparked during the first loading cycle (with the stress fields defined in Section 2.2) and thus the model assumes a fully debonded state (see Section 2.4.3) for all loading cycles $N > 0$.

2.4.2. Crack propagation phase

During the crack propagation phase, the stress fields in a level-[1] bundle with one broken fibre are presented in Figure 4, where it is assumed that an interfacial crack propagates symmetrically to the mid-plane defined by the fibre-break (as observed experimentally [1]), in a self-similar way. Consequently, the effective recovery length is composed by two regions, separated by a crack-tip at $|x| = a^{[0]}/2$:

i) near the break in fibre $\mathcal{A}$ ($|x| < a^{[0]}/2$), the interface is debonded and no longer transfers

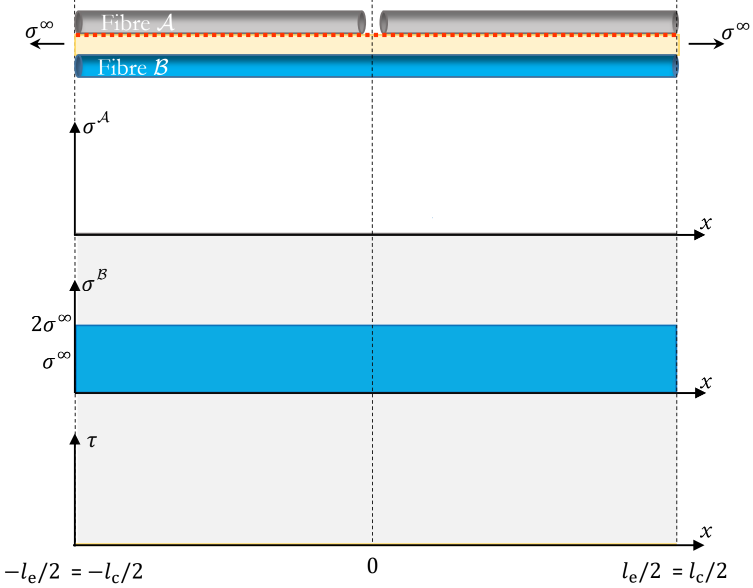

Figure 5: Stress fields and length scales in a fully debonded level-[1] bundle.

shear stresses between the broken fibre (which is under no longitudinal stresses, $\sigma^{\mathcal{A}} = 0$) and the surviving fibre (which is under a uniform stress $\sigma^{\mathcal{B}} = 2\sigma^{\infty}$). The debonded area grows according the to the Paris law (previously defined in Eq. 10);

ii) between the crack-tip and the end of the recovery region ($a^{[0]}/2 < |x| \leq l_{\mathrm{e}}^{[0]}/2$), the interface is damaged, but still transfer shear stresses between the two fibres $\mathcal{A}$ and $\mathcal{B}$. The length of the damaged region remains constant during the propagation phase, at the value $l_{\mathrm{K}}^{[0]}$ previously calculated in Eq. 14.

This analysis can also be applied to calculate the effective recovery length during the crack propagation phase around a broken sub-bundle of any level-$[i]$:

$$\frac{l_{\mathrm{e}}^{[i]}(\sigma_{\mathrm{peak}}^{\infty}, R^{\infty}, N)}{2} = \frac{l_{\mathrm{K}}^{[i]}(\sigma_{\mathrm{crt}}^{\infty\,[i]})}{2} + \frac{1}{P^{[i]}} \cdot \frac{\mathrm{d}A^{[i]}}{\mathrm{d}N}(\sigma_{\mathrm{peak}}^{\infty}, R^{\infty}) \cdot (N - N_{\mathrm{init}}^{[i]}). \tag{16}$$

The end of the crack propagation phase occurs when the effective recovery length reaches the length of the specimen l_{spec}. Therefore, the number of cycles of the propagation phase ($\mathit{\Delta} N_{\mathrm{prop}}^{[i]}$) is calculated by

$$\frac{l_{\mathrm{spec}}}{2} = \frac{l_{\mathrm{K}}^{[i]}(\sigma_{\mathrm{crt}}^{\infty\,[i]})}{2} + \frac{1}{P^{[i]}} \cdot \frac{\mathrm{d}A^{[i]}}{\mathrm{d}N}(\sigma_{\mathrm{peak}}^{\infty}, R^{\infty}) \cdot \mathit{\Delta} N_{\mathrm{prop}}^{[i]} \quad \Leftrightarrow \quad \mathit{\Delta} N_{\mathrm{prop}}^{[i]} = \frac{\left(l_{\mathrm{spec}} - l_{\mathrm{K}}^{[i]}(\sigma_{\mathrm{crt}}^{\infty\,[i]})\right) \cdot P^{[i]}}{2 \cdot \frac{\mathrm{d}A^{[i]}}{\mathrm{d}N}(\sigma_{\mathrm{peak}}^{\infty}, R^{\infty})}. \tag{17}$$

2.4.3. *Fully debonded phase*

When the interfacial crack reaches the length of the specimen, the bundle enters the fully debonded phase, where the surviving sub-bundle (fibre $\mathcal{B}$ in Figure 5) is the one carrying the total remote load applied to the bundle (see Figure 5). In this phase, the effective recovery length is limited by the physical length of the specimen, and therefore remains unchanged during further fatigue cycles (i.e. $l_{\mathrm{e}}^{[i]}(\sigma_{\mathrm{peak}}^{\infty}, R^{\infty}, N \geq N_{\mathrm{debond}}^{[i]}) = l_{\mathrm{spec}}$, with $N_{\mathrm{debond}}^{[i]} = N_{\mathrm{init}}^{[i]} + \mathit{\Delta} N_{\mathrm{prop}}^{[i]}$).

TABLE 1: Calculation of length scales for the different phases of the fatigue life; the effective recovery length $l_\mathrm{e}^{[i]}$ is calculated from the Paris law in Eq. 13.

Length scales	$N=0$	$0<N\leq N_\mathrm{init}^{[i]}$	$N_\mathrm{init}^{[i]}<N\leq N_\mathrm{debond}^{[i]}$	$N\geq N_\mathrm{debond}^{[i]}$
$l_\mathrm{K}^{[i]}(\sigma_\mathrm{peak}^\infty,R^\infty,N)$	$l_\mathrm{e}^{[i]}(\sigma_\mathrm{peak}^\infty,0)$	$l_\mathrm{e}^{[i]}(\sigma_\mathrm{peak}^\infty,R^\infty,N)$	$l_\mathrm{K}^{[i]}$ (Eq. 14)	0
$a^{[i]}(\sigma_\mathrm{peak}^\infty,R^\infty,N)$	0	0	$l_\mathrm{e}^{[i]}(\sigma_\mathrm{peak}^\infty,R^\infty,N)-l_\mathrm{K}^{[i]}$	l_spec
$l_\mathrm{c}^{[i+1]}(\sigma_\mathrm{peak}^\infty,R^\infty,N)$	$2\cdot l_\mathrm{e}^{[i]}(\sigma_\mathrm{peak}^\infty,0)$	$2\cdot l_\mathrm{e}^{[i]}(\sigma_\mathrm{peak}^\infty,R^\infty,N)$	if $l_\mathrm{e}^{[i]}\leq l_\mathrm{spec}/2$: $2\cdot l_\mathrm{e}^{[i]}(\sigma_\mathrm{peak}^\infty,R^\infty,N)$; if $l_\mathrm{e}^{[i]}>l_\mathrm{spec}/2$: l_spec	l_spec

2.4.4. Scaling law

Due to continuous changes in the phases of the bundles with increasing loading cycles (see Figures 2, 4 and 5), the static scaling law derived in the literature for the initial static case [32] is not valid for fatigue loading. Therefore, a general scaling law valid for all phases of the fatigue analysis will be derived in this section. For the sake of a simplicity, the survival probabilities $S^{[i]}$ are represented only as functions of the applied remote peak stress (hereby represented only as σ^∞), although they are calculated for each cycle N of the fatigue analysis and also depend on the loading ratio R^∞; the dependency of the length scales ($l_\mathrm{e}^{[i]}$, $l_\mathrm{K}^{[i]}$, $a^{[i]}$ and $l_\mathrm{c}^{[i]}$ defined in Table 1) on these same variables will also be omitted.

The scaling law calculates the survival probability of a level-$[i+1]$ bundle within the bundle control length $l_\mathrm{c}^{[i+1]}$. The survival probabilities of the level-$[i]$ sub-bundles used as inputs are calculated at the associated recovery length $l_\mathrm{e}^{[i]}$ by

$$\ln S_{\mathrm{U,e}}^{[i]}(\sigma^\infty)=\frac{l_\mathrm{e}^{[i]}(\sigma^\infty)}{l_0^\mathrm{f}}\cdot\ln S_{\mathrm{U},0}^{[i]}(\sigma^\infty),\tag{18}$$

where $S_{\mathrm{U},0}^{[i]}(\sigma^\infty)$ is the survival probability of a level-$[i]$ sub-bundle under a uniform remote stress σ^∞ with a length l_0^f. The scaling law considers two possible survival scenarios of the level-$[i+1]$ bundle:

- both level-$[i]$ sub-bundles are able to withstand the uniform remote stress σ^∞ within the level-$[i+1]$ control length. The probability of this scenario is given by the WLT, considering that the level-$[i+1]$ bundle of length $l_\mathrm{c}^{[i+1]}$ contains 2 level-$[i]$ sub-bundles

$$S_{\mathcal{U}}^{[i+1]}(\sigma^\infty)=\left[S_{\mathrm{U,e}}^{[i]}(\sigma^\infty)^{\frac{l_\mathrm{c}^{[i+1]}}{l_\mathrm{e}^{[i]}}}\right]^2;\tag{19a}$$

- one level-$[i]$ sub-bundle breaks under the remote stress, and the neighbouring level-$[i]$ sub-bundle is able to withstand the resulting stress concentrations. The probability of this scenario is given by

$$S_{\mathcal{K}}^{[i+1]}(\sigma^\infty)=2\cdot\underbrace{[1-S_{\mathrm{U,e}}^{[i]}(\sigma^\infty)^{\frac{l_\mathrm{c}^{[i+1]}}{l_\mathrm{e}^{[i]}}}]}_{\mathrm{I}}\cdot\underbrace{S_{\mathrm{U,e}}^{[i]}(2\sigma^\infty)^{\frac{a^{[i]}}{l_\mathrm{e}^{[i]}}}}_{\mathrm{II}}\cdot\underbrace{S_{\mathrm{K,e}}^{[i]}(\sigma^\infty)^{\frac{l_\mathrm{K}^{[i]}}{l_\mathrm{e}^{[i]}}}}_{\mathrm{III}}\cdot\underbrace{S_{\mathrm{U,e}}^{[i]}(\sigma^\infty)^{\frac{l_\mathrm{c}^{[i+1]}-l_\mathrm{e}^{[i]}}{l_\mathrm{e}^{[i]}}}}_{\mathrm{IV}},\tag{19b}$$

where the exponents in each term of Eq. 19a and 19b are defined in Table 1.

In Eq. 19b, term I corresponds to the failure probability of the weakest level-$[i]$ sub-bundle under the uniform stress σ^{∞} within the level-[i+1] control length; term II corresponds to the survival probability of the surviving level-[i] sub-bundle under a uniform stress $2\sigma^{\infty}$ within the debonded length $a^{[i]}$; term III corresponds to the survival probability of the surviving level-[i] sub-bundle under the stress concentrations field within the interface damaged region (with length $l_{\mathrm{K}}^{[i]}$, defiend in Table 1); term IV corresponds to the survival probability of the surviving level-[i] sub-bundle under the uniform remote stress σ^{∞}, outside the recovery region of the broken level-[i] sub-bundle (i.e. within the length in which a break in the surviving sub-bundle would interact with the break in the weakest sub-bundle).

The stress fields in a level-[i] sub-bundle were determined by considering a cohesive interfacial law (Eq. 6); however, in order to calculate the survival probability in term III ($S_{\mathrm{K,e}}^{[i]}(\sigma^{\infty})$) analytically, a linear approximation of the stress field in the surviving sub-bundle (defined in Eq. 6c) was made, as detailed in Appendix B. Using this linear approximation, the term $S_{\mathrm{K,e}}^{[i]}(\sigma^{\infty})$ is given by [32]:

$$\begin{aligned} &\ln[S_{\mathrm{K,e}}^{[i]}(\sigma^{\infty})] = \frac{l_{\mathrm{e}}^{[i]}}{l_0^{\mathrm{f}}} \cdot \frac{k \cdot \ln[S_{\mathrm{L,0}}^{[i]}(k \cdot \sigma^{\infty}) - \ln[S_{\mathrm{L,0}}^{[i]}(\sigma^{\infty})]}{k-1} \quad \text{, with} \\ &\ln[S_{\mathrm{L,0}}^{[i]}(\sigma)] = \frac{1}{\sigma} \int_{\sigma_{\mathrm{L}}=0}^{\sigma} \ln[S_{\mathrm{U,0}}^{[i]}(\sigma_{\mathrm{L}})]\mathrm{d}\sigma_{\mathrm{L}} \;\; \text{and} \;\; k=2. \end{aligned} \tag{20}$$

It should be noted that, while this simplification leads to linear stress concentrations in the surviving sub-bundle within the interface damaged region (as previously obtained with a perfectly-plastic interface law [32]) the length of the interface damaged region calculated with the cohesive law ($l_{\mathrm{K}}^{[i]}$ defined in Table 1) is still larger than the one predicted using a perfectly-plastic interface, hence justifying the new derivations in Section 2.2, even for the static case.

Both scenarios in Eq. 19a and 19b are mutually exclusive, and therefore their probabilities can be added to define the general scaling law, which is valid for every phase of the fatigue analysis:

$$S_{\mathrm{U,c}}^{[i+1]}(\sigma^{\infty}) = S_{\mathrm{U,e}}^{[i]}(\sigma^{\infty})^{\frac{2l_{\mathrm{c}}^{[i+1]}}{l_{\mathrm{e}}^{[i]}}} + 2 \cdot [1 - S_{\mathrm{U,e}}^{[i]}(\sigma^{\infty})^{\frac{l_{\mathrm{c}}^{[i+1]}}{l_{\mathrm{e}}^{[i]}}}] \cdot S_{\mathrm{U,e}}^{[i]}(2\sigma^{\infty})^{\frac{a^{[i]}}{l_{\mathrm{e}}^{[i]}}} \cdot S_{\mathrm{K,e}}^{[i]}(\sigma^{\infty})^{\frac{l_{\mathrm{K}}^{[i]}}{l_{\mathrm{e}}^{[i]}}} \cdot S_{\mathrm{U,e}}^{[i]}(\sigma^{\infty})^{\frac{l_{\mathrm{c}}^{[i+1]} - l_{\mathrm{e}}^{[i]}}{l_{\mathrm{e}}^{[i]}}}. \tag{21}$$

During the different phases of the fatigue life of a level-[$i+1$] bundle, the scaling law can be simplified as follows:

- initiation phase: $a^{[i]} = 0 \quad \wedge \quad l_{\mathrm{c}}^{[i+1]} = 2 \cdot l_{\mathrm{e}}^{[i]}$:

$$S_{\mathrm{U,c}}^{[i+1]}(\sigma^{\infty}) = S_{\mathrm{U,e}}^{[i]}(\sigma^{\infty})^4 \cdot [1 - S_{\mathrm{U,e}}^{[i]}(\sigma^{\infty})^2] \cdot S_{\mathrm{K,e}}^{[i]}(\sigma^{\infty}) \cdot S_{\mathrm{U,e}}^{[i]}(\sigma^{\infty}); \tag{22a}$$

- propagation phase: $a^{[i]} > 0 \quad \wedge \quad l_{\mathrm{c}}^{[i+1]} = 2 \cdot l_{\mathrm{e}}^{[i]}$:

$$S_{\mathrm{U,c}}^{[i+1]}(\sigma^{\infty}) = S_{\mathrm{U,e}}^{[i]}(\sigma^{\infty})^4 + 2 \cdot [1 - S_{\mathrm{U,e}}^{[i]}(\sigma^{\infty})^2] \cdot S_{\mathrm{U,e}}^{[i]}(2\sigma^{\infty})^{\frac{a^{[i]}}{l_{\mathrm{e}}^{[i]}}} \cdot S_{\mathrm{K,e}}^{[i]}(\sigma^{\infty})^{\frac{l_{\mathrm{K}}^{[i]}}{l_{\mathrm{e}}^{[i]}}} \cdot S_{\mathrm{U,e}}^{[i]}(\sigma^{\infty}); \tag{22b}$$

- fully debonded phase: $l_{\mathrm{c}}^{[i+1]} = l_{\mathrm{e}}^{[i]} = a^{[i]}$:

$$S_{\mathrm{U,c}}^{[i+1]}(\sigma^{\infty}) = S_{\mathrm{U,e}}^{[i]}(\sigma^{\infty})^2 + 2 \cdot [1 - S_{\mathrm{U,e}}(\sigma^{\infty})] \cdot S_{\mathrm{U,e}}^{[i]}(2\sigma^{\infty}). \tag{22c}$$

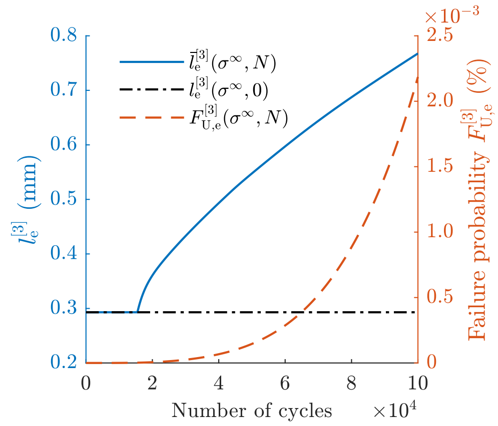

Figure 6: Evolution of the effective recovery length within a level-[4] bundle (i.e. interfacial crack propagating around a level-[3] sub-bundle) after the averaging process (using the inputs defined in Tables 2-4 associated to the material system T/D, with $\sigma^{\infty}_{\mathrm{peak}} = 2.5$ GPa and $R^{\infty} = 0.1$).

2.4.5. *Effective recovery length averaging*

An interfacial crack in a level-$[i+1]$ bundle can only initiate after a level-$[i]$ sub-bundle break occurs. Therefore, if a level-$[i]$ sub-bundle breaks during (for instance) the 2$^{\mathrm{nd}}$ remote fatigue cycle ($j = 2$), with associated probability $\Delta F_{\mathrm{U,e}}^{[i]}(\sigma^{\infty}, j = 2) = F_{\mathrm{U,e}}^{[i]}(\sigma^{\infty}, j = 2) - F_{\mathrm{U,e}}^{[i]}(\sigma^{\infty}, j = 1)$, the level-$[i]$ interfacial crack has grown for only 1 fatigue cycle by the remote fatigue cycle $N = 3$. Considering the possibilities of the level-$[i]$ sub-bundle breaking at the remote cycles $j = \{0, 1, 2, 3\}$, then the *averaged* effective recovery length ($\bar{l}_{\mathrm{e}}^{[i]}$) at the end of the 3$^{\mathrm{rd}}$ fatigue cycle ($N = 3$) is given by

$$\begin{aligned} \bar{l}_{\mathrm{e}}^{[i]}(\sigma^{\infty}, 3) = \Big[& l_{\mathrm{e}}^{[i]}(\sigma^{\infty}, 3) \cdot \Delta F_{\mathrm{U,e}}^{[i]}(\sigma^{\infty}, 0) + l_{\mathrm{e}}^{[i]}(\sigma^{\infty}, 2) \cdot \Delta F_{\mathrm{U,e}}^{[i]}(\sigma^{\infty}, 1) \; + \\ & l_{\mathrm{e}}^{[i]}(\sigma^{\infty}, 1) \cdot \Delta F_{\mathrm{U,e}}^{[i]}(\sigma^{\infty}, 2) + l_{\mathrm{e}}^{[i]}(\sigma^{\infty}, 0) \cdot \Delta F_{\mathrm{U,e}}^{[i]}(\sigma^{\infty}, 3) \Big] / F_{\mathrm{U,e}}^{[i]}(\sigma^{\infty}, 3), \end{aligned} \tag{23}$$

with

$$\Delta F_{\mathrm{U,e}}^{[i]}(\sigma^{\infty}, j) = \begin{cases} F_{\mathrm{U,e}}^{[i]}(\sigma^{\infty}, 0) & \text{for } j = 0, \\ F_{\mathrm{U,e}}^{[i]}(\sigma^{\infty}, j) - F_{\mathrm{U,e}}^{[i]}(\sigma^{\infty}, j-1) & \text{for } j \geq 1. \end{cases} \tag{24}$$

The outcome of this process is represented in Figure 6, where one can see that the averaged effective recovery length of the a level-[3] sub-bundle remains constant and equal to its static value $l_{\mathrm{e}}^{[3]}(\sigma^{\infty}, 0)$ until the failure probability of level-[3] sub-bundles ($F_{\mathrm{U,e}}^{[3]}$) starts increasing. The averaging of the effective recovery length can be generalised to any number N of fatigue cycles by

$$\bar{l}_{\mathrm{e}}^{[i]}(\sigma^{\infty}, N) = \frac{\sum_{j=1}^{N} \left[l_{\mathrm{e}}^{[i]}(\sigma^{\infty}, N - j + 1) \cdot \Delta F_{\mathrm{U,e}}^{[i]}(\sigma^{\infty}, j) \right]}{F_{\mathrm{U,e}}^{[i]}(\sigma^{\infty}, N)}. \tag{25}$$

2.5. *Model implementation*

The model presented in the previous sections was implemented in Matlab, and an overview of the numerical implementation is presented in Figure 7.

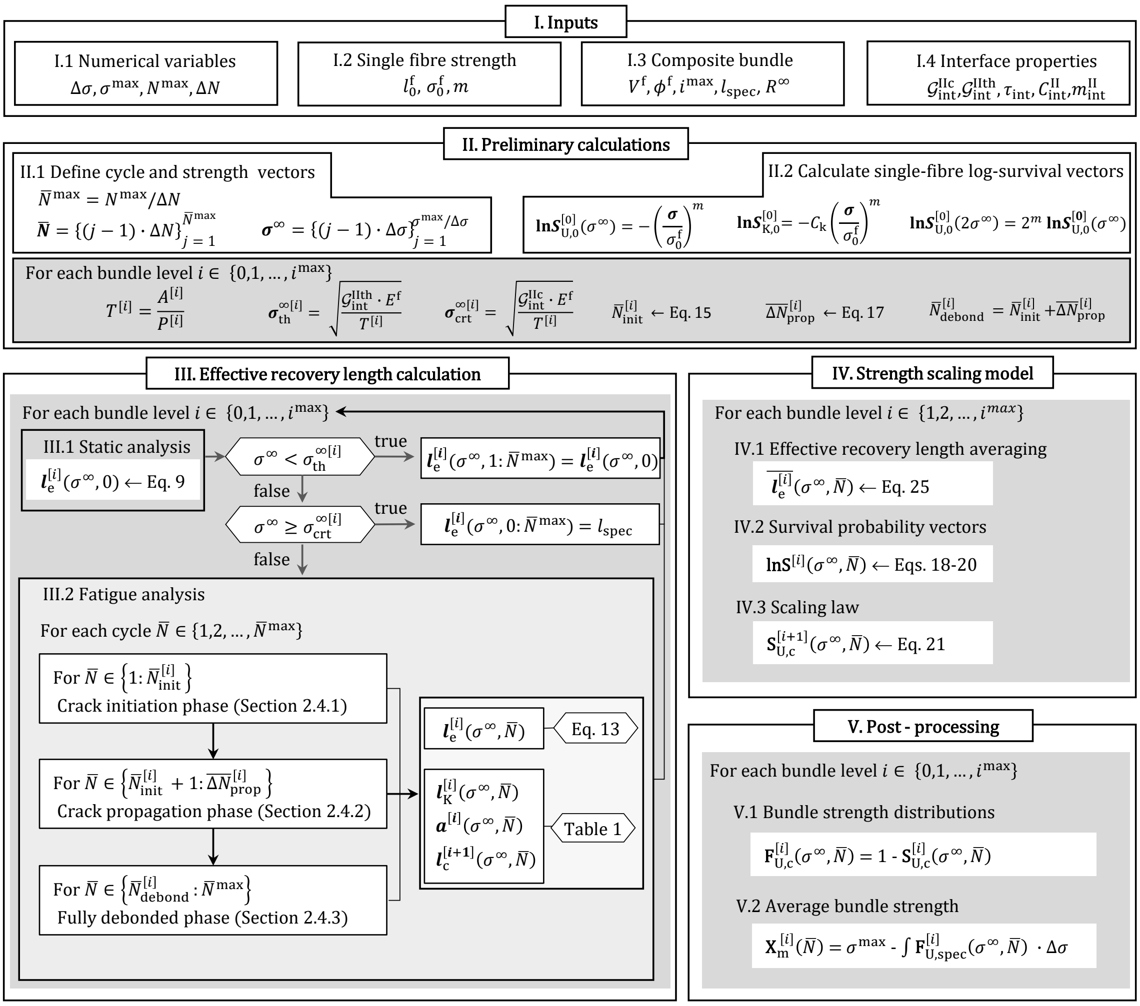

Figure 7: Schematic representation of the numerical implementation of the model.

3. Results

3.1. Static results

Figure 8a compares predictions for the static strength distribution $X_{\mathrm{m}}^{[i]}(N=0)$ obtained by the present model (considering a linear cohesive behaviour for the interface) against those obtained by the original version of the HSL available in the literature [32] (using a perfectly-plastic interface behaviour), considering the same input values as in Table 1 of the paper presenting the static HSL [32], and a mode-II fracture toughness of the interface $\mathcal{G}_{\mathrm{int}}^{\mathrm{IIc}} = 1$ kJ/m^2. The results show that considering a cohesive behaviour and a finite fracture toughness for the interface leads to lower predictions of the static bundle strength compared to the results assuming a perfectly-plastic behaviour, albeit the difference is small. Furthermore, the influence of assuming linear stress concentration fields in the fibres rather than the full analytical solution (presented in Appendix B) is shown to be small, which ensures the accuracy of the approximation considered in Eq. 20.

Figure 8b shows that the relation between the effective recovery length and the applied remote stress is no longer linear when a cohesive behaviour for the interface is considered, in opposition to the linear relation found for a perfectly-plastic interface behaviour. Furthermore, the non-linear evolution of the effective recovery length is more pronounced as the remote stress approaches the critical value $\sigma_{\mathrm{crt}}^{\infty}$.

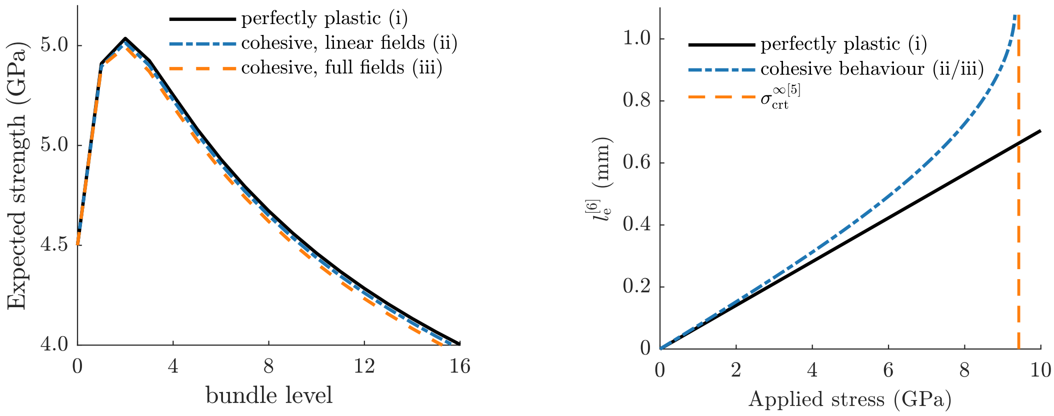

(a) Size effect on the expected static strength.

(b) Effective recovery length of a level-[6] sub-bundle.

Figure 8: Static analysis assuming different behaviours of the interface: i) perfectly-plastic behaviour [32]; ii) cohesive behaviour and linear approximation of the stress fields in the sub-bundle; iii) cohesive behaviour and analytical stress fields in the sub-bundle (see Appendix B for the difference between (ii) and (iii)).

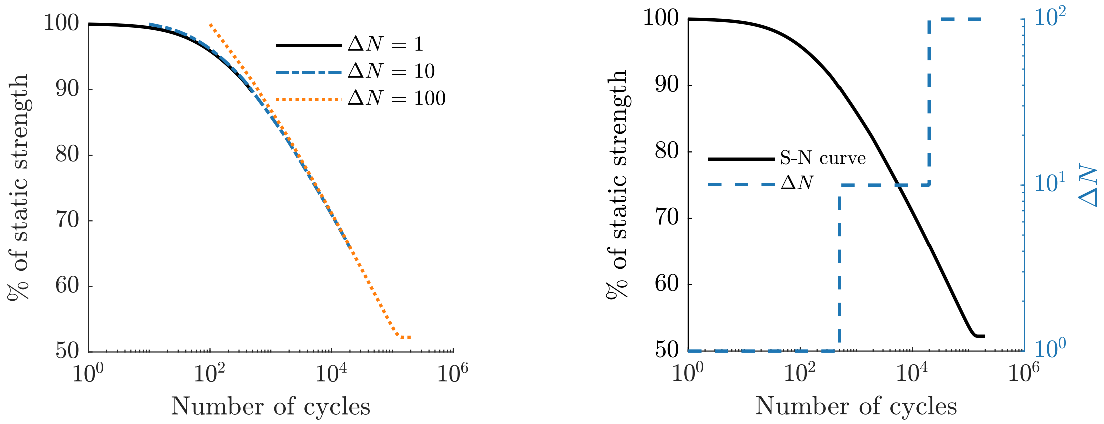

(a) Expected S-N curve obtained with different values of the cycle jump ΔN.

(b) Expected S-N curve obtained with the adaptive cycle jump scheme.

Figure 9: Convergence analysis of the model with the adaptive cycle jump scheme.

3.2. Convergence study

The model inputs for the convergence study presented in this section and for the parametric study detailed in Section 3.3 are the ones presented for the A/P fibre/matrix combination in Tables 2-4 which were selected to represent the experimental results of Gamstedt and Talreja [1]. Figure 9a shows that the model requires small cycle jumps (ΔN) in order to accurately calculate the S-N curve in the region of low cycle fatigue, and progressively converges for larger cycle jumps as the number of applied cycles increases. In order to maximize the computational efficiency of the model, the numerical implementation of the model detailed in Figure 7 was combined with an adaptive cycle jump scheme, where the cycle jump is gradually increased throughout the analysis, as shown in Figure 9b. With this adaptive scheme, the whole S-N curve shown in Figure 9b can be obtained accurately within a model runtime of less than 60 seconds.

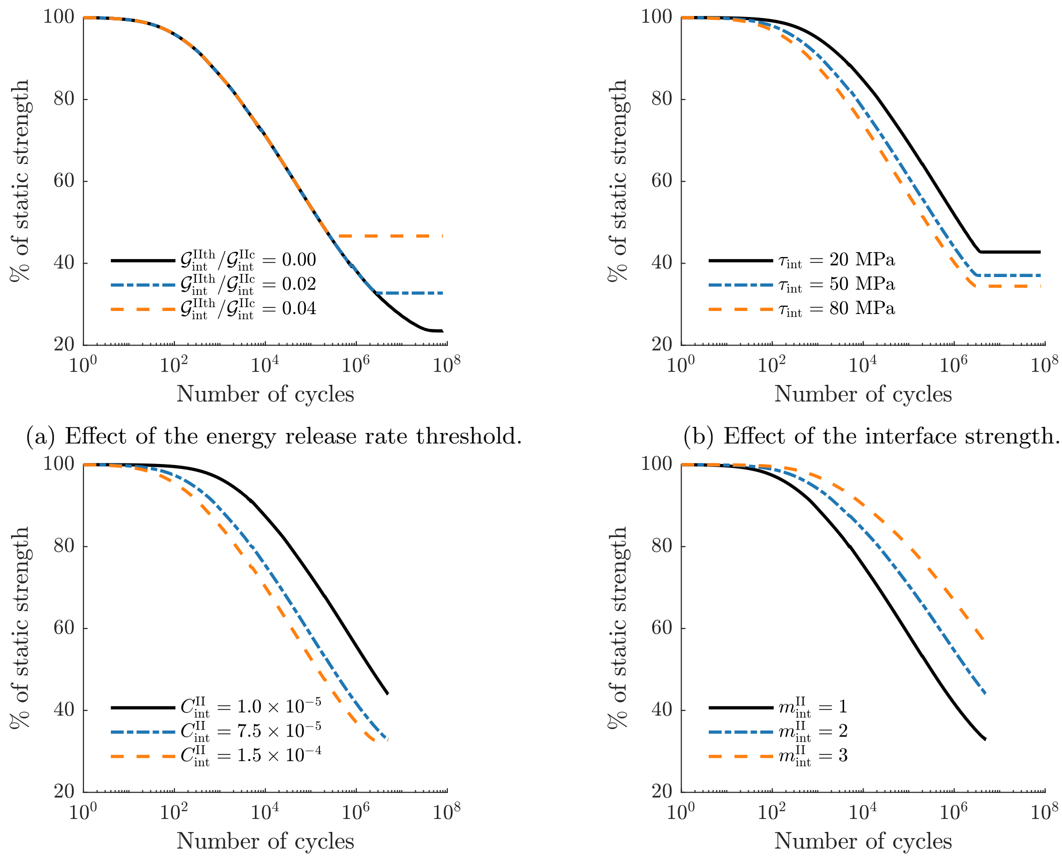

(a) Effect of the energy release rate threshold.

(b) Effect of the interface strength.

(c) Effect of the $C_{\text{int}}^{\text{II}}$ Paris law constant.

(d) Effect of the $m_{\text{int}}^{\text{II}}$ Paris law constant.

Figure 10: Parametric study on the expected S-N curve predicted by the model.

3.3. Parametric study

Figure 10a shows that $\mathcal{G}_{\text{int}}^{\text{IIth}}$ influences the fatigue life limit (or the region of no failure) in the S-N curves of UD composites: as $\mathcal{G}_{\text{int}}^{\text{IIth}}$ increases, the peak remote stress associated with the fatigue life limit also increases. This is in good agreement with the framework presented by Talreja [15], where the lower band of the fatigue life diagram of UD composites under longitudinal tension is associated with the fatigue limit of the interface.

Figure 10b describes the influence of the interface's shear strength τ_{int} on the expected fatigue behaviour of UD composite bundles, where bundles with stronger interfaces show a more pronounced strength degradation due to fatigue. This creates a trade-off between the fatigue life and static strength of UD composites under longitudinal tension, as it has been demonstrated that stronger interfaces lead to higher values of the static strength [32]. The absolute value of the fatigue life limit of bundles remains unchanged for different values of τ_{int}, although this is not clear in Figure 10b due to the normalisation of the fatigue results relatively to the expected static strength of the specimen (which is different for each value of τ_{int}).

Figures 10c and 10d demonstrate that the Paris law constants of the interface ($C_{\text{int}}^{\text{II}}$ and $m_{\text{int}}^{\text{II}}$) have a significant influence in the expected S-N curves of UD composites under longitudinal tension, as they directly affect the debond growth (see Eq. 10 and 13) and, consequently, the stress redistribution in the sub-bundles and in the interface.

The fatigue life of specimens with different number of fibres (represented by different levels-[i]) are shown as colour map in Figure 11a . Above the predicted specimen static strength $X_{\text{m}}^{[i]}$, the

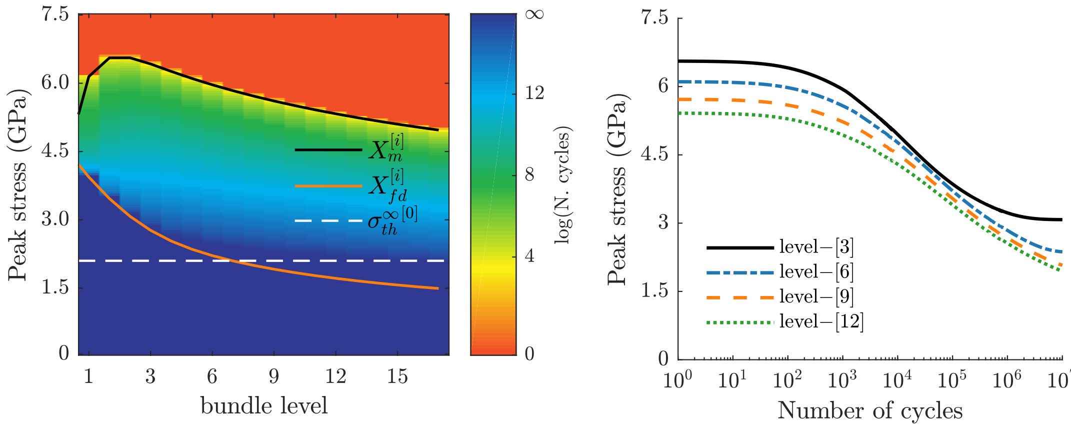

(a) S-N colour map of different bundle levels.

(b) Size effect on the S-N curve for different bundle levels.

Figure 11: Size-effects on the expected S-N curves predicted by the model, for the `A/P` material defined in Tables 2-4.

predicted number of cycles to failure is zero (i.e. the specimen will fail in the first loading cycle), as expected. Below a certain value of the peak applied stress, the model predicts an infinite fatigue life limit that can occur in one of the two following cases:

(i) no bundle of level $j < i$ is expected to fail, as be the peak remote stress applied is lower than the strength of a fully debonded specimen $X_{\mathrm{fd}}^{[i]}$ (obtained by Eq. 22c); this case defines the fatigue life limit for small (i.e low level) specimens;

(ii) no interfacial crack growth occurs, as the peak remote stress applied is lower than the threshold stress value below which the interface near a fibre-break does not accumulate any damage ($\sigma_{\mathrm{th}}^{\infty\,[0]}$, Eq. 12); this case defines the fatigue life limit for large (i.e high level) specimens.

Figure 11b shows the existence of size effects in the fatigue life of composite specimens, where smaller specimens present faster and higher degradation in their fatigue strength than the large ones. Furthermore, smaller specimens also present an infinite fatigue life limit at higher remote stress values, due to the higher average static strength in the fully debonded case ($X_{\mathrm{fd}}^{[i]}$, which governs the fatigue life limit of small bundles, as explained in point (i) above.)

3.4. Validation against experimental results

Material and input parameters considered for all the subsequent model validation cases are shown in Tables 2 - 4. Figure 12 validates the model against the experimental results of Meziere et al. [9], where different values for the Weibull parameters of the fibres (each obtained from single-fibre tensile tests at different gauge lengths l_0^{f}) were considered [52]. For all sets of Weibull parameters originally measured in the literature, the S-N curves predicted by the model show a good correlation with the experimental results; interestingly the correlation is optimal with the combination of Weibull parameters that more accurately predicted the average static strength of the specimen measured experimentally.

Figure 13a shows a colour map with the stochastic S-N curves predicted by the model, as well as the experimental results obtained by Khatibi [6]. The experimental results obtained by Gamstedt and Talreja [1], presented in the form of a fatigue life diagram (where the cyclic peak strain is plotted against the number of cycles), are compared with the model predictions in Figure 13b.

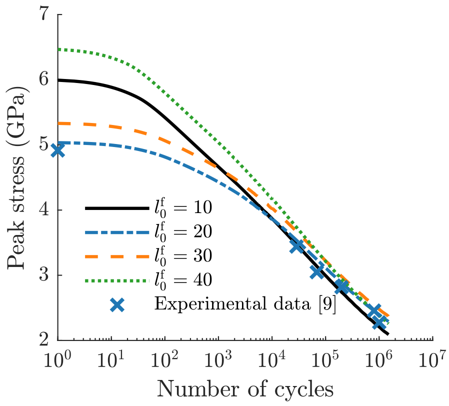

Figure 12: Validation of the expected S-N curves predicted by the model against a set of experimental results [9], and analysis of the effect of the Weibull parameters (measured at different gauge length l_0^f, see Table 3) on the predicted S-N curve. Model inputs are defined in Tables 2-4 (for the T/D fibre/matrix combination).

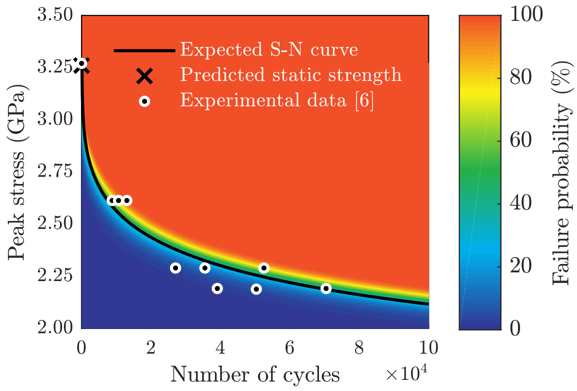

(a) Stochastic S-N curve and validation against experimental results [6]. Model inputs are defined in Tables 2-4 (for the G/R fibre/matrix combination).

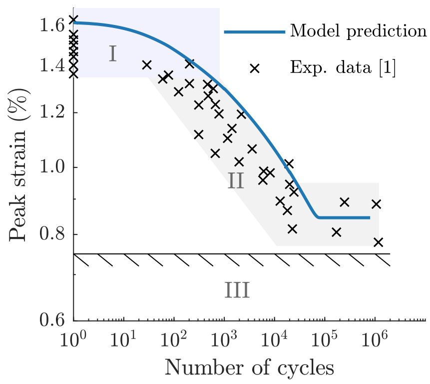

(b) Fatigue life diagram and validation against experimental results [1]. Model inputs are defined in Tables 2-4 (for the A/P fibre/matrix combination).

Figure 13: Validation of the model against experimental results.

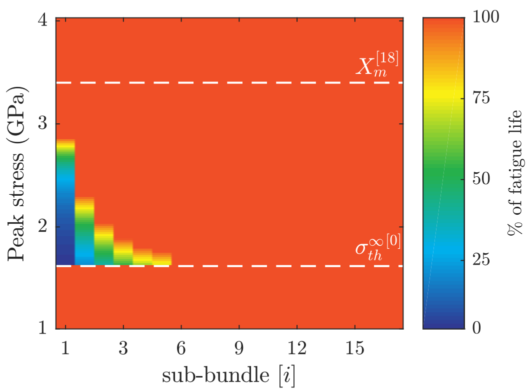

(a) Crack initiation.

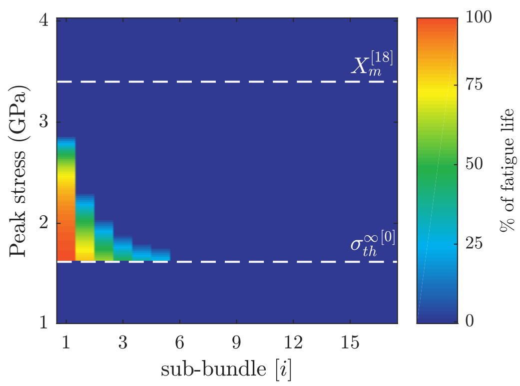

(b) Crack propagation.

Figure 14: Expected duration of the crack initiation and propagation phases (for several sub-bundle levels-$[i]$) in the overall fatigue life of the level-[18] bundle analysed in Figure 13b.

TABLE 2: Nominal model inputs for validation against experimental results.

Exp. results	Fibre ref.	Interface ref.	$n^{[i]}$	V^{f} (%)	l_{spec}(mm)	R^{∞}
[9]	`T`†	`D`‡	10^5	60	180	0.1
[6]	`G`†	`R`‡	10^6	60	195	0.1
[1]	`A`†	`P`‡	10^5	60	127	0.1

† See Table 3 for detailed description.
‡ See Table 4 for detailed description.

TABLE 3: Fibre properties for model validation; for fibre type `T`, Deng et al. [52] provide 4 sets of Weibull parameters for the single-fibre strength distribution, measured at 4 different fibre lengths l_0^{f}.

Fibre ref.	Fibre type	E^{f}(GPa)	ϕ^{f}(µm)	l_0^{f}(mm)	m	σ_0^{f}(GPa)	Reference
`T`	T700	230	7.00	10	3.5	7.700	[52]
				20	5.0	6.200	[52]
				30	5.0	6.200	[52]
				40	3.7	6.000	[52]
`G`	G34-700	226	7.00	30	5.2	3.800	[52]
`A`	AS4	222	6.85	10	4.8	4.493	[53]

TABLE 4: Interface properties for model validation.

Interface ref.	τ_{int}(MPa)	$\mathcal{G}_{\mathrm{int}}^{\mathrm{IIc}}$(kJ/m^2)	$\mathcal{G}_{\mathrm{int}}^{\mathrm{IIth}}$(kJ/m^2)	$C_{\mathrm{int}}^{\mathrm{II}}$(mm^2/cycle)	$m_{\mathrm{int}}^{\mathrm{II}}$	Reference
`D`†	70	1	0.02*	1.0×10^{-3}*	2.0*	[9]
`R`†	70	1	0.025*	3.0×10^{-3}*	2.2*	[6]
`P`†	110	2	0.025*	2.0×10^{-3}*	2.0*	[1, 54]

† `D` - Diglycidyl Ether of Bisphenol-A (DGEBA) epoxy fibre-break; `R` - RIGIDITE© 5228 toughened epoxy; `P` - APC-2-PEEK toughened thermoplastic fibre-break.
* Estimated values.

4. Discussion

4.1. Physical phenomena predicted by the model

The model captures many characteristic features of the fatigue behaviour of UD composites under longitudinal tension:

a) The threshold value of the energy release rate $\mathcal{G}_{\mathrm{int}}^{\mathrm{IIth}}$ of the interface is an important parameter for the fatigue life of UD composite specimens, as it defines the infinite fatigue life region (Figure 10a). This parameter influences the peak remote stress required to propagate an interfacial crack around a single fibre-break ($\sigma_{\mathrm{th}}^{\infty[0]}$ in Figure 11a), which triggers the fatigue damage mechanism. Removing the threshold value (i.e setting $\mathcal{G}_{\mathrm{int}}^{\mathrm{IIth}} = 0$) reduces the fatigue limit to the stress value that statistically causes no fibre-breaks ($X_{\mathrm{fd}}^{[i]}$ in Figure 11a), in which case no fatigue occurs because there are no initiation points for interfacial cracks to develop.

b) The results of the developed model, when presented in the form of a fatigue life diagram (Figure 13b), clearly show the existence of three distinct regions, which have been reported and discussed in the literature [1, 15]. In region I, almost no fatigue damage is accumulated (leading to a horizontal orientation of the S-N curve), which demonstrates that the failure mechanism of a UD composite is dominated by fibre failure; region II is dominated by the fatigue degradation process, where the growth of interfacial debonds from fibre- or sub-bundle-breaks is the main fatigue damage mechanism. Finally, region III defines a fatigue limit below which failure does not occur, and where interfacial cracks either do not initiate, or have a rate of propagation to slow to lead to failure. The model is also able to recreate the main features captured by the experimental results (Figures 12 and 13).

c) The model results indicate that specimen failure at remote peak stresses close to the static strength is dominated by fibre-breaks, without the existence of any stable crack initiation or propagation at any sub-bundle level (Figure 14). Figure 14b also demonstrates that, as the applied peak stress decreases, crack propagation from individual fibre-breaks and small broken sub-bundles starts occurring for most of the fatigue life of a specimen; for even lower values of the applied peak stress, progressively larger sub-bundle-breaks form early in the fatigue life of the specimen, with interface cracks propagating for the majority of the fatigue life. Nevertheless, Figure 14b also shows that there is no stable initiation and propagation of interfacial cracks from broken sub-bundles above a certain number of fibres (level-[6] in Figure 14, which corresponds to a cluster of 64 fibres); this suggests the existence of a critical cluster size under fatigue loading, which could possibly be different from the one associated with static loading [55], although further analysis would be required in order to accurately define the critical cluster size under fatigue.

4.2. Uncertainty in model inputs and their influence in the predicted fatigue behaviour

There are certain model inputs whose availability in the literature is scarce. Therefore, the influence of these inputs and the importance of determining them experimentally are discussed below:

a) The values of $\mathcal{G}_{\text{int}}^{\text{IIth}}$ used for the validation of the model (Table 3) are slightly lower than values considered by other authors when studying delamination under fatigue loading, which are typically around 0.1 kJ/m^2 [39, 56, 57]. This difference in the values of $\mathcal{G}_{\text{int}}^{\text{IIth}}$ considered in Section 3 can be justified by the different fatigue mechanism in the present analysis (which govern interfacial crack propagation around single-fibre or sub-bundle breaks), compared to the one characterised in most experiments (corresponding to the propagation of cracks between plies which typically contain a resin-rich region, and which corresponds to fatigue delamination). This difference is also corroborated by Hojo et al. [28], who studied interfacial fatigue crack propagation using bi-fibre shear specimens and found that the threshold to fatigue crack growth of the fibre interface is lower than that to fatigue delamination in composite laminates.

b) The Weibull parameters of the strength distribution of single-fibres have a significant influence in the model results, particularly in the static strength predicted by the model (Figure 13b). Furthermore, the Weibull shape parameter m has a noticeable influence in the slope of the S-N curves, as shown in Figure 12. These results reveal the importance of accurately measuring the Weibull strength distribution of fibres experimentally.

c) The Paris law constants of the interface ($C_{\text{int}}^{\text{II}}$ and $m_{\text{int}}^{\text{II}}$) have an important effect on the composite S-N curves predicted by the model. Despite the lack of experimental results to determine these constants for interfacial debonding, an estimation of these parameters was made (see Table 4) based on values found in the literature [16, 23–27] for mode-II delamination propagation. This motivated the parametric study presented in Section 3.3 to demonstrate the sensitivity of the model to these parameters.

5. Conclusions

An analytical Hierarchical Scaling Law to predict the behaviour of composite fibre bundles under tension-tension fatigue was developed, implemented and validated against experimental results. The main conclusions of this work are as follows:

- The analytical formulation of the HSL, in combination with an adaptive jump cycle strategy, allows one to perform a stochastic analysis of the fatigue life of composite fibre bundles in a very efficient way; S-N curves can be obtained for a range of specimen sizes and different failure probabilities in a run-time of less than 60 seconds.

- The model shows good agreement when validated against different sets of experimental results [1, 6, 9], and is able to capture the characteristic trends of the fatigue behaviour of UD composites reported in the literature [15], as well as predicting the variability inherent to the experimental results.

- The debond growth was assumed to follow a Paris power law, whose constants have an important influence in the predicted S-N curves. Despite the lack of experimentally measured constants for the materials studied, the ones used for the model validation lie within the range of values found in the literature for mode-II fatigue delamination propagation. Nevertheless, determining the Paris law constants experimentally for mode-II debond growth in composites would be essential, as it would allow for a more accurate prediction and understanding of the fatigue behaviour of UD composites.

The developed model is an efficient predictive tool for the fatigue behaviour of UD composites and associated size effects, and therefore we expect it to be applicable in the following scenarios:

- in an academic environment, the model can be used to provide quantitative information and detailed insight of the fatigue mechanisms in UD composites;

- for material development, the model can be used to evaluate the impact of improving constituent properties (e.g. improving the bonding between fibres and matrix, or decreasing the scatter in fibre-strength) on the evolution of the fatigue degradation of UD composites;

- for structural design and reliability, the model can be used to predict the scatter associated with fatigue life, and to scale fatigue tests from lab-scale specimens to large structures, thus reducing the cost and time required for experimental characterisation of materials and qualification of structures.

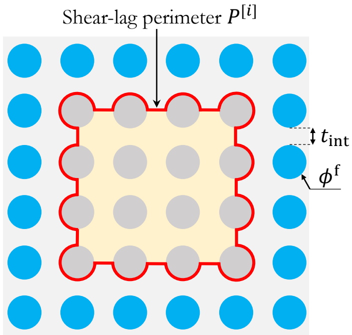

Figure 15: Shear lag perimeter of a level-[i] sub-bundle when considering a square fibre-packing and preferential interfacial failure [32].

Acknowledgments

The research leading to these results has been done within the framework of the FiBreMoD project and has received funding from the European Union's Horizon 2020 research and innovation programme under the Marie Sklodowska-Curie grant agreement no. 722626. S. Pimenta also acknowledges the support from the Royal Academy of Engineering in the scope of her Research Fellowship on 'Multiscale discontinuous composites for large scale and sustainable structural applications' (2015-2019).

Appendix A Geometry of the cross-section of a fibre bundle

A level-[i] sub-bundle with a fibre diameter ϕ^{f} and fibre volume fraction V^{f} has the following cross-sectional area (solely based on the fibres):

$$A^{[i]} = n^{[i]} \cdot A^{\text{f}}, \qquad A^{\text{f}} = \pi \frac{\left(\phi^{\text{f}}\right)^2}{4}. \tag{A.1}$$

Considering a square fibre-packing and preferential interfacial failure (Figure 15), the shear-lag perimeter $P^{[i]}$ of the sub-bundle is [32]:

$$\begin{aligned} &P^{[i]} = 3 \cdot P^{\text{f}} + 4 \cdot \left[\left(\sqrt{n^{[i]}} - 1\right) \cdot t_{\text{int}} + \left(\sqrt{n^{[i]}} - 2\right) \cdot \frac{P^{\text{f}}}{2}\right], \qquad \text{with} \\ &P^{\text{f}} = \pi \cdot \phi^{\text{f}} \qquad \text{and} \qquad t_{\text{int}} = \left(\frac{\sqrt{\pi}}{2 \cdot \sqrt{V^{\text{f}}}} - 1\right) \cdot \phi^{\text{f}}. \end{aligned} \tag{A.2}$$

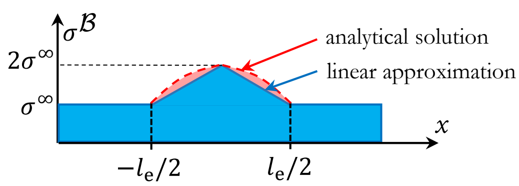

Figure 16: Comparison between the linear approximation and the analytical solution of stress concentration stress fields in the surviving fibre/sub-bundle $\mathcal{B}$.

Appendix B Linear approximation to non-uniform stress fields near fibre/sub-bundle breaks

Figure 16 shows the difference between (i) the analytical stress fields when a surviving fibre/sub-bundle undergoes non-uniform stress concentrations (Eq. 6c) and (ii) a linear approximation of those stress fields, which were assumed in the model (see Section 2.4.4). According to Eq. 6c, the actual (i.e. non-linear) stress fields in the surviving fibre/sub-bundle after the static loading cycle are

$$\sigma^{\mathcal{B}}(x) = \sigma^{\infty} + \frac{\tau_{\text{int}}}{\lambda^{[i]} T^{[i]}} \sin\Big(\lambda^{[i]} \Big[\frac{l_{\text{e}}^{[i]}}{2} - x\Big]\Big), \quad \text{for } |x| < l_{\text{e}}^{[i]}(\sigma^{\infty}, R^{\infty}, 0). \tag{B.3}$$

Following the WLT extended to non-uniform stresses [32], the survival probability of the fibre/sub-bundle under $\sigma^{\mathcal{B}}(x)$ ($S_{\text{K},0}(\sigma^{\infty})$) can be calculated from

$$\ln[S_{\text{K},0}^{[i]}(\sigma^{\infty})] = \frac{2}{l_{\text{e}}^{[i]}(\sigma^{\infty})} \int_{x=0}^{\frac{l_{\text{e}}^{[i]}}{2}} \ln[S_{\text{U},0}^{[i]}(\sigma^{\mathcal{B}})] \mathrm{d}x. \tag{B.4a}$$

Changing the integration variable to $\sigma^{\mathcal{B}}$,

$$x = \frac{1}{\lambda^{[i]}} \cdot \text{asin}\Big(\frac{\lambda^{[i]} \cdot T^{[i]}[\sigma^{\mathcal{B}} - \sigma^{\infty}]}{\tau_{\text{int}}}\Big) \Rightarrow \mathrm{d}x = \frac{T^{[i]}}{\tau_{\text{int}}\sqrt{1 - \frac{[(\sigma^{\mathcal{B}} - \sigma^{\infty}) \cdot \lambda^{[i]} \cdot T^{[i]}]^2}{(\tau_{\text{int}})^2}}} \mathrm{d}\sigma^{\mathcal{B}}, \tag{B.4b}$$

thus

$$\ln[S_{\text{K,e}}^{[i]}(\sigma^{\infty})] = \frac{l_{\text{e}}^{[i]}}{l_0^{\text{f}}} \cdot \frac{T^{[i]}}{\tau_{\text{int}} \cdot \frac{l_{\text{e}}^{[i]}}{2}} \int_{\sigma^{\mathcal{B}}=\sigma^{\infty}}^{2\sigma^{\infty}} \frac{\ln[S_{\text{U},0}^{[i]}(\sigma^{\mathcal{B}})]}{\sqrt{1 - \Big[\frac{(\sigma^{\mathcal{B}} - \sigma^{\infty}) \cdot \lambda^{[i]} \cdot T^{[i]}}{(\tau_{\text{int}})}\Big]^2}} \mathrm{d}\sigma^{\mathcal{B}}. \tag{B.4c}$$

This expression can be used to evaluate $\ln[S_{\text{K,e}}^{[i]}(\sigma^{\infty})]$ numerically, considering the non-linear stress field $\sigma^{\mathcal{B}}(x)$ defined in Eq. 6c and B.3. This allows us to assess the accuracy of the linear approximation made in Eq. 20 to calculate $\ln[S_{\text{K,e}}^{[i]}(\sigma^{\infty})]$, with the results shown in Figure 8a.

References

[1] E. K. Gamstedt and R. Talreja, “Fatigue damage mechanisms in unidirectional carbon-fibre-reinforced plastics,” *Journal of Materials Science*, vol. 34, no. 11, pp. 2535–2546, 1999.

[2] E. K. Gamstedt, L. A. Berglund, and T. Peijs, “Fatigue mechanisms in unidirectional glass-fibre-reinforced polypropylene,” *Composites Science and Technology*, vol. 59, no. 5, pp. 759–768, 1999.

[3] H. Kim, “Axial fatigue failure sequence and mechanisms in unidirectional fiberglass composites,” *Journal of Composite Materials*, vol. 12, no. 2, pp. 139–152, 1978.

[4] Y. Al-Assaf and H. El Kadi, “Fatigue life prediction of unidirectional glass fiber/epoxy composite laminae using neural networks,” *Composite Structures*, vol. 53, no. 1, pp. 65–71, 2001.

[5] Y. Shan and K. Liao, “Environmental fatigue behavior and life prediction of unidirectional glass-carbon/epoxy hybrid composites,” *International Journal of Fatigue*, vol. 24, no. 8, pp. 847–859, 2002.

[6] A. Afaghi-Khatibi and Y.-W. Mai, “Characterisation of fibre/matrix interfacial degradation under cyclic fatigue loading using dynamic mechanical analysis,” *Composites Part A: Applied Science and Manufacturing*, vol. 33, no. 11, pp. 1585 – 1592, 2002.

[7] Y. Shan, K. F. Lai, K. T. Wan, and K. Liao, “Static and dynamic fatigue of glass–carbon hybrid composites in fluid environment,” *Journal of Composite Materials*, vol. 36, no. 2, pp. 159–172, 2002.

[8] Y. Zhou, "Fatigue strength characterization of E-glass fibers using fiber bundle test," *Journal of Composite Materials*, vol. 38, no. 22, pp. 2025–2035, 2004.

[9] Y. Meziere, A. R. Bunsell, Y. Favry, J. Teissedre, and A. T. Do, "Large strain cyclic fatigue testing of unidirectional carbon fibre reinforced epoxy resin," *Composites Part A: Applied Science and Manufacturing*, vol. 36, pp. 1627–1636, 2005.

[10] M. Quaresimin, L. Susmel, and R. Talreja, "Fatigue behaviour and life assessment of composite laminates under multiaxial loadings," *International Journal of Fatigue*, vol. 32, no. 1, pp. 2 – 16, 2010. Fourth International Conference on Fatigue of Composites (ICFC4).

[11] J. R. A. Tost, F. Heinrich, "Novel test method for characterization of unidirectional composite fatigue properties," in *European Conference on Composite Materials - ECCM17*, (Munich, Germany), June 2016.

[12] S. M. O. Tavares and P. M. S. T. de Castro, "An overview of fatigue in aircraft structures," *Fatigue & Fracture of Engineering Materials & Structures*, 2017.

[13] A. Somer and A. Bunsell, "The tensile and fatigue behaviour of carbon fibres," *Plastics Rubber Composites Processign and Applications*, vol. 18, p. 263, 1992.

[14] E. K. Gamstedt, "Effects of debonding and fiber strength distribution on fatigue-damage propagation in carbon fiber-reinforced epoxy," *Journal of Applied Polymer Science*, vol. 76, no. 4, pp. 457–474, 2000.

[15] R. Talreja and C. V. Singh, *Damage and Failure of Composite Materials*. Cambridge University Press, 2012.

[16] A. Pupurs, S. Goutianos, P. Brondsted, and J. Varna, "Interface debond crack growth in tension-tension cyclic loading of single fiber polymer composites," *Composites Part A: Applied Science and Manufacturing*, vol. 44, pp. 86 – 94, 2013.

[17] P. A. Gradin and J. Backlund, "Fatigue debonding in fibrous composites," *International Journal of Adhesion and Adhesives*, pp. 154–158, 1981.

[18] A. DiBenedetto, "Measurement of the thermomechanical stability of interphases by the embedded single fiber test," *Composites Science and Technology*, vol. 42, no. 1, pp. 103 – 123, 1991. Special Issue Interfaces in Composites.

[19] R. A. Latour, J. Black, and B. Miller, "Fatigue behaviour characterization of the fibre-matrix interface," *Journal of Materials Science*, vol. 24, pp. 3616–3620, Oct 1989.

[20] A. Pupurs and J. Varna, "Unidirectional composite in mechanical fatigue: modelling debond growth from fibre breaks," *Plastics, Rubber and Composites*, vol. 39, no. 3-5, pp. 128–136, 2010.

[21] A. Afaghi-Khatibi, L. Ye, and Y.-W. Mai, "An experimental study of the influence of fibrematrix interface on fatigue tensile strength of notched composite laminates," *Composites Part B: Engineering*, vol. 32, no. 4, pp. 371 – 377, 2001.

[22] B. Large-Toumi, M. Salvia, and L. Vincent, "Fiber matrix interface effect on monotonic and fatigue behavior of unidirectional carbon epoxy composites," *ASTM International*, pp. 182–200, 1996.

[23] A. Amiri-Rad, M. Mashayekhi, and F. P. van der Meer, "Cohesive zone and level set method for simulation of high cycle fatigue delamination in composite materials," *Composite Structures*, vol. 160, pp. 61 – 69, 2017.

[24] L. F. Kawashita and S. R. Hallett, "A crack tip tracking algorithm for cohesive interface element analysis of fatigue delamination propagation in composite materials," *International Journal of Solids and Structures*, vol. 49, no. 21, pp. 2898 – 2913, 2012.

[25] R. Brighenti, A. Carpinteri, and D. Scorza, "Micromechanical crack growth-based fatigue damage in fibrous composites," *International Journal of Fatigue*, vol. 82, pp. 98 – 109, 2016. Fatigue at all Scales.

[26] L. Carreras, J. Renart, A. Turon, J. Costa, Y. Essa, and F. M. de la Escalera, "An efficient methodology for the experimental characterization of mode ii delamination growth under fatigue loading," *International Journal of Fatigue*, vol. 95, pp. 185 – 193, 2017.

[27] R. Panduranga and K. Shivakumar, "Mode-II total fatigue life model for unidirectional IM7/8552 carbon/epoxy composite laminate," *International Journal of Fatigue*, vol. 94, pp. 97 – 109, 2017.

[28] M. Hojo, Y. Matsushita, M. Tanaka, and T. Adachi, "Interfacial fatigue crack propagation in microscopic model composite using bifiber shear specimens," *Composites Part A: Applied Science and Manufacturing*, vol. 43, no. 2, pp. 239–246, 2012.

[29] B. W. Rosen, "Tensile failure of fibrous composites," *AIAA Journal*, vol. 2, pp. 169–177, 1964.

[30] Y. Swolfs, L. Gorbatikh, V. Romanov, S. Orlova, S. Lomov, and I. Verpoest, "Stress concentrations in an impregnated fibre bundle with random fibre packing," *Composites Science and Technology*, vol. 74, pp. 113 – 120, 2013.

[31] A. de Morais, "Prediction of the longitudinal tensile strength of polymer matrix composites," *Composites Science and Technology*, vol. 66, no. 15, pp. 2990 – 2996, 2006.

[32] S. Pimenta and S. T. Pinho, "Hierarchical scaling law for the strength of composite fibre bundles," *Journal of the Mechanics and Physics of Solids*, vol. 61, no. 6, pp. 1337–1356, 2013.

[33] S. Behzadi, P. T. Curtis, and F. R. Jones, "Improving the prediction of tensile failure in unidirectional fibre composites by introducing matrix shear yielding," *Composites Science and Technology*, vol. 69, no. 14, pp. 2421 – 2427, 2009. The Sixteenth International Conference on Composite Materials with Regular Papers.

[34] Y. Swolfs, R. M. McMeeking, I. Verpoest, and L. Gorbatikh, "Matrix cracks around fibre breaks and their effect on stress redistribution and failure development in unidirectional composites," *Composites Science and Technology*, vol. 108, pp. 16 – 22, 2015.

[35] W. I. Newman and A. M. Gabrielov, "Failure of hierarchical distributions of fibre bundles. 1," *International Journal of Fracture*, vol. 50, pp. 1–14, Jul 1991.

[36] "The statistical theory of the strength of bundles of threads. i," *Proceedings of the Royal Society of London A: Mathematical, Physical and Engineering Sciences*, vol. 183, no. 995, pp. 405–435, 1945.

[37] C. Qian, T. Westphal, and R. P. Nijssen, "Micro-mechanical fatigue modelling of unidirectional glass fibre reinforced polymer composites," *Computational Materials Science*, vol. 69, pp. 62–72, 2013.

[38] P. Robinson, U. Galvanetto, D. Tumino, G. Bellucci, and D. Violeau, "Numerical simulation of fatigue-driven delamination using interface elements," *International Journal for Numerical Methods in Engineering*, vol. 63, no. 13, pp. 1824–1848, 2005.

[39] A. Turon, J. Costa, P. P. Camanho, and C. G. Dávila, "Simulation of delamination in composites under high-cycle fatigue," *Composites Part A: Applied Science and Manufacturing*, vol. 38, no. 11, pp. 2270–2282, 2007.

[40] P. W. Harper and S. R. Hallett, "A fatigue degradation law for cohesive interface elements – Development and application to composite materials," *International Journal of Fatigue*, vol. 32, no. 11, pp. 1774–1787, 2010.

[41] L. F. Kawashita and S. R. Hallett, "A crack tip tracking algorithm for cohesive interface element analysis of fatigue delamination propagation in composite materials," *International Journal of Solids and Structures*, vol. 49, no. 21, pp. 2898–2913, 2012.

[42] B. L. Bak, A. Turon, E. Lindgaard, and E. Lund, "A benchmark study of simulation methods for high-cycle fatigue-driven delamination based on cohesive zone models," *Composite Structures*, vol. 164, pp. 198–206, 2017.

[43] S. L. Ogin, "A model for the fatigue life and residual strength of unidirectional and cross-ply composite materials which fail by "wear-out" ," in *Fibre reinforced composites, 3rd International Conference*, (Liverpool, England), March, 1988.

[44] S. Garcea, I. Sinclair, and S. Spearing, "Fibre failure assessment in carbon fibre reinforced polymers under fatigue loading by synchrotron X-ray computed tomography," *Composites Science and Technology*, vol. 133, pp. 157 – 164, 2016.

[45] S. Pinho, P. Robinson, and L. Iannucci, "Fracture toughness of the tensile and compressive fibre failure modes in laminated composites," *Composites Science and Technology*, vol. 66, no. 13, pp. 2069 – 2079, 2006.

[46] S. Pimenta and S. T. Pinho, "An analytical model for the translaminar fracture toughness of fibre composites with stochastic quasi-fractal fracture surfaces," *Journal of the Mechanics and Physics of Solids*, vol. 66, pp. 78 – 102, 2014.

[47] G.W.Weibull, "A statistical distribution function of wide applicability," *Journal of Applied Mechanics*, pp. 293 – 197, 1951.

[48] C. M. Landis and R. M. McMeeking, "A shear-lag model for a broken fiber embedded in a composite with a ductile matrix," *Composites Science and Technology*, vol. 59, no. 3, pp. 447–457, 1999.

[49] S. Spearing, P. Beaumont, and M. Ashby, "Fatigue damage mechanics of composite materials. ii: A damage growth model," *Composites Science and Technology*, vol. 44, no. 2, pp. 169 – 177, 1992.

[50] S. Pimenta and P. Robinson, "An analytical shear-lag model for composites with 'brick-and-mortar' architecture considering non-linear matrix response and failure," *Composites Science and Technology*, vol. 104, pp. 111–124, 2014.

[51] S. Spearing, P. Beaumont, and M. Ashby, "Fatigue damage mechanics of composite materials. II: A damage growth model," *Composites Science and Technology*, vol. 44, pp. 169–177, 1992.

[52] S. Deng, L. Ye, Y.-W. Mai, and H.-Y. Liu, "Evaluation of fibre tensile strength and fibre/matrix adhesion using single fibre fragmentation tests," *Composites Part A: Applied Science and Manufacturing*, vol. 29, no. 4, pp. 423–434, 1998.

[53] I. J. Beyerlein and S. L. Phoenix, "Statistics for the strength and size effects of microcomposites with four carbon fibers in epoxy resin," *Composites Science and Technology*, vol. 56, no. 1, pp. 75–92, 1996.

[54] "TenCate Advanced Composites. Datasheet: TenCate Cetex(R) TC1200 PEEK resin system," 2013, (accessed in December 2017).

[55] S. Pimenta, "A computationally efficient hierarchical scaling law to predict damage accumulation in composite fibre bundles," *Composites Science and Technology*, vol. 146, pp. 210–225, 2017.

[56] E. Armanios, R. Bucinell, D. Wilson, L. Asp, A. Sjogren, and E. Greenhalgh, "Delamination growth and thresholds in a carbon/epoxy composite under fatigue loading," *Journal of Composites Technology and Research*, vol. 23, no. 2, p. 55, 2001.

[57] H. Masaki, O. Shojiro, C. G. Gustafson, and T. Keisuke, "Effect of matrix resin on delamination fatigue crack growth in CFRP laminates," *Engineering Fracture Mechanics*, vol. 49, no. 1, pp. 35–47, 1994.